Spin-Orbital Texture in Topological Insulators

Haijun Zhang,[1] Chao-Xing Liu,[2] and Shou-Cheng Zhang[1]

[1]*Department of Physics, McCullough Building, Stanford University, Stanford, California 94305-4045, USA*
[2]*Department of Physics, The Pennsylvania State University, University Park, Pennsylvania 16802-6300, USA*

(Received 22 November 2012; published 5 August 2013)

For three-dimensional topological insulators in the Bi_2Se_3 family, topological surface states with p_z orbitals have a left-handed spin texture for the upper Dirac cone and a right-handed spin texture for the lower Dirac cone. In this work, we predict a new form of the spin-orbital texture associated with the p_x and p_y orbitals. For the upper Dirac cone, a left-handed (right-handed) spin texture is coupled to the "radial" ("tangential") orbital texture, whereas for the lower Dirac cone, the coupling of spin and orbital textures is the exact opposite. The "tangential" ("radial") orbital texture is dominant for the upper (lower) Dirac cone, leading to the right-handed spin texture for the in-plane orbitals of both the upper and lower Dirac cones. A spin-resolved and photon polarized angle-resolved photoemission spectroscopy experiment is proposed to observe this novel spin-orbital texture.

DOI: 10.1103/PhysRevLett.111.066801 PACS numbers: 73.20.−r, 71.18.+y, 73.21.−b

Three-dimensional topological insulators (TIs) are new states of quantum matter with helical gapless surface states consisting of an odd number of Dirac cones inside the bulk band gap protected by time-reversal symmetry (TRS) [1–4]. The underlying physical origin of the topological property of TIs is the strong spin-orbit coupling (SOC), which plays a similar role as the Lorentz force in the quantum Hall state. Due to the SOC interaction, the spin and momentum are locked to each other, forming a spin texture in the momentum space for the surface states of TIs [5–7]. The spin texture has been directly observed in spin-resolved angle-resolved photon emission spectroscopy (spin-resolved ARPES) [8–12]. The spin texture gives rise to a nontrivial Berry phase for the topological surface states and suppresses the backscatterings under TRS, leading to possible device applications in spintronics.

Besides the spin texture, it has also been shown recently that the atomic **p** orbitals of the Bi_2Se_3 family of topological insulators form a pattern in the momentum space, dubbed as the orbital texture, for the topological surface states [13,14]. In this work, we find that the orbital texture found in Refs. [13,14] is actually not separated from the spin texture and predict a coupled spin-orbital texture for the topological surface states. Based on both the effective $\mathbf{k}\cdot\mathbf{p}$ theory and *ab initio* calculations, we find, besides the usual locking between the electron spin and the crystal momentum, the spin texture is also locked to the atomic orbital texture, which is dubbed as the "spin-orbital texture." We show that p_z orbitals have left-handed spin texture for the upper Dirac cone and right-handed spin texture for the lower Dirac cone, sharing the same feature as the total spin texture of the surface states. In contrast, the in-plane orbitals (p_x and p_y orbitals) reveal more intriguing features: for the upper Dirac cone of surface states, a "radial" orbital texture is coupled to a left-handed spin texture and a "tangential" orbital texture is coupled to a right-handed spin texture. For the lower Dirac cone, the coupling between spin and orbital textures is exactly opposite. An electron spin-resolved and photon polarized ARPES experiment is proposed to observe this novel spin-orbital texture of the surface states of TIs.

The surface states of TIs are described by the Dirac type of effective Hamiltonian [5,15]

$$H_{\mathrm{surf}}(k_x, k_y) = \hbar v_f(\sigma^x k_y - \sigma^y k_x), \tag{1}$$

with the Fermi velocity v_f and Pauli matrix σ. The hexagonal warping effect [16] is ignored, which has distinct influence only in the large momentum region, but here we are more interested in the low energy physics with small momentum. The salient feature of this effective Hamiltonian is the "spin-momentum locking," which means for a fixed momentum $\mathbf{k}$, the "spin," denoted by the Pauli matrix σ, has a fixed direction for the eigenstate of the Hamiltonian. Since the "spin" is always perpendicular to the momentum, we can introduce a helicity operator, defined as $\hat{h} = (1/k)\hat{z}\cdot(\vec{k}\times\vec{\sigma})$ which commutates with the Hamiltonian, to determine the handness of the "spin" texture. For the upper Dirac cone of surface states, the helical operator $\hat{h} = -1$, leading to a left-handed "spin" texture in the momentum space while for the lower Dirac cone, $\hat{h} = 1$ yields a right-handed "spin" texture. However, one should note that here the "spin" is not the real spin, but the total angular momentum $\vec{J} = \vec{S} + \vec{L}$, which is a combination of the real spin $\vec{S}$ and the orbital angular momentum $\vec{L}$ due to SOC. Consequently, the basis of the surface effective Hamiltonian (1) are denoted as $|\Psi_{J_z=\pm(1/2)}\rangle$ with the lower indices $\pm(1/2)$ representing the total angular momentum along the z direction. In order to understand what is the texture for the real spin $\vec{S}$, it is necessary to write down the explicit form of the basis wave function $|\Psi_{\pm(1/2)}\rangle$.

The form of the basis $|\Psi_{\pm(1/2)}\rangle$ can be constructed by symmetry considerations. Generally the basis $|\Psi_{\pm(1/2)}\rangle$ depends on the momentum $\mathbf{k}$ and we can expand it up to the first order in $\mathbf{k}$ as $|\Psi_{\pm(1/2)}\rangle = |\Psi^{(0)}_{\pm(1/2)}\rangle + |\Psi^{(1)}_{\pm(1/2)}\rangle$. Here we are only interested in the $\mathbf{p}$ orbitals of Bi and Se atoms in the topological insulator Bi_2Se_3 and can decompose the zeroth-order wave function as

$$|\Psi^{(0)}_{\pm(1/2)}\rangle = \sum_{\alpha}[u_{0,\alpha}|\alpha, p_z, \uparrow(\downarrow)\rangle + v_{0,\alpha}|\alpha, p_{\pm}, \downarrow(\uparrow)\rangle] \quad (2)$$

and the first-order wave function as

$$|\Psi^{(1)}_{\pm(1/2)}\rangle = \sum_{\alpha}[\pm k_{\pm}(iu_{1,\alpha}|\alpha, p_{\mp}, \uparrow(\downarrow)\rangle + iv_{1,\alpha}|\alpha, p_z, \downarrow(\uparrow)\rangle) \mp iw_{1,\alpha}k_{\mp}|\alpha, p_{\pm}, \uparrow(\downarrow)\rangle], \quad (3)$$

where $k_{\pm} = k_x \pm ik_y$, $|\uparrow\rangle$ and $|\downarrow\rangle$ denote the spin, $|p_z\rangle$ and $|p_{\pm}\rangle = \mp(1/\sqrt{2})(|p_x\rangle \pm i|p_y\rangle)$ denote different p orbitals, and α denotes indices other than the spin and orbital, such as atom indices. The above wave functions are constructed by conserving the z-direction total angular momentum J_z. For example, for the first term in (3), $k_{\pm}$, $|p_{\mp}\rangle$, and $|\uparrow(\downarrow)\rangle$ carry the angular momentum ± 1, ∓ 1, $\pm(1/2)$, respectively, so the z-direction total angular momentum is $\pm(1/2)$. It is easy to know that the other terms in (3) also carry the z-direction total angular momentum $\pm(1/2)$. More details about the form of the wave functions can be found in the online Supplemental Material [17]. $u_{0(1),\alpha}$, $v_{0(1),\alpha}$ and $w_{1,\alpha}$ are material-dependent parameters. By comparing with the *ab initio* calculations, we can take them to be real. $|\Psi_{(1/2)}\rangle$ and $|\Psi_{-(1/2)}\rangle$ are related to each other by TRS. The expressions of the basis (2) and (3) can be substituted into the eigen wave functions of the Hamiltonian (1), $|\Phi_{\pm}\rangle = (1/\sqrt{2})[\pm ie^{-i\theta_k}|\Psi_{(1/2)}\rangle + |\Psi_{-(1/2)}\rangle]$, yielding the following forms of the wave functions:

$$|\Phi_{+}\rangle = \sum_{\alpha}\Big[(u_{0,\alpha} - v_{1,\alpha}k)|\alpha, p_z, \uparrow_\theta\rangle - \frac{i}{\sqrt{2}}(v_{0,\alpha} - u_{1,\alpha}k - w_{1,\alpha}k)|\alpha, p_r, \uparrow_\theta\rangle + \frac{1}{\sqrt{2}}(v_{0,\alpha} - u_{1,\alpha}k + w_{1,\alpha}k)|\alpha, p_t, \downarrow_\theta\rangle\Big], \quad (4)$$

$$|\Phi_{-}\rangle = \sum_{\alpha}\Big[(u_{0,\alpha} + v_{1,\alpha}k)|\alpha, p_z, \downarrow_\theta\rangle + \frac{i}{\sqrt{2}}(v_{0,\alpha} + u_{1,\alpha}k + w_{1,\alpha}k)|\alpha, p_r, \downarrow_\theta\rangle - \frac{1}{\sqrt{2}}(v_{0,\alpha} + u_{1,\alpha}k - w_{1,\alpha}k)|\alpha, p_t, \uparrow_\theta\rangle\Big]. \quad (5)$$

Here $\vec{k} = (k, \theta_k)$, $|\uparrow_\theta(\downarrow_\theta)\rangle = (1/\sqrt{2})(+(-)ie^{-i\theta_k}|\uparrow\rangle + |\downarrow\rangle)$ stands for the left-handed (right-handed) helical spin texture and $|p_r\rangle = \cos\theta_k|p_x\rangle + \sin\theta_k|p_y\rangle$, $|p_t\rangle = -\sin\theta_k|p_x\rangle + \cos\theta_k|p_y\rangle$ are the radial and tangential orbital textures, as shown in Figs. 1(a) and 1(b), respectively. From the expressions (4) and (5), we can clearly see that the $|p_z\rangle$ orbital is coupled to the left-handed spin texture $|\uparrow_\theta\rangle$ for the upper Dirac cone and the right-handed spin texture $|\downarrow_\theta\rangle$ for the lower Dirac cone. Furthermore, for the upper Dirac cone, the radial orbital texture $|p_r\rangle$ is always coupled to the left-handed spin texture $|\uparrow_\theta\rangle$ and the tangential orbital texture $|p_t\rangle$ is always coupled to the right-handed spin texture $|\downarrow_\theta\rangle$. The situation is exactly opposite for the lower Dirac cone.

The expressions (4) and (5) are the main analytical results of this Letter, which show explicitly the spin-orbital texture. This tells us that one cannot separate the spin texture from the orbital texture in this system due to the strong spin-orbit coupling. To confirm our analytical results, the *ab initio* method is adopted to calculate the projection of surface states on the spin and orbital basis, defined by the quantity

$$D^{\pm}_{i,\eta} = \langle\Phi_{\pm}|(|p_i\rangle\langle p_i| \otimes s_\eta)|\Phi_{\pm}\rangle, \quad (6)$$

where $p_i = p_x, p_y, p_z$ for the three $\mathbf{p}$ orbitals, $s_0 = \mathbf{1}_{2\times 2}$ denotes the charge part and $s_{x,y,z}$ denote the three Pauli matrices for the spin. In the following, we will compare the analytical calculation of the intensity $D^{\pm}_{i,\eta}$ with *ab initio* calculations.

The Vienna *ab initio* simulation package (VASP) [18,19] is employed to carry out *ab initio* calculations with the framework of the Perdew-Burke-Ernzerhof-type [20] generalized gradient approximation of density functional theory [21]. Projector augmented wave pseudopotentials are used for all of the calculations in this work [22]. $10 \times 10 \times 10$ and $10 \times 10 \times 1$ are used for the $\mathbf{k}$-grid of bulk and freestanding calculations, respectively. The kinetic energy cutoff is fixed to 450 eV. Six quintuple layers are fixed in the supercell for freestanding calculations, and the thickness of vacuum is taken to be 50 Å. The lattice constant and the atomic parameters are directly obtained from experiments. SOC is included with the non-self-consistent

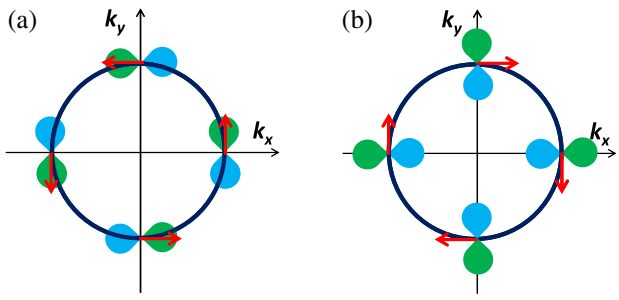

FIG. 1 (color online). (a),(b) The tangential orbital texture with the right-handed helical spin texture (a) and the radial orbital texture with the left-handed helical spin texture (b) for the upper Dirac cone.

calculation. In order to compare with the result of the ARPES experiments, the projections of all the orbitals are only for the first Se and Bi atoms on the top surface of the freestanding model.

The surface states of Bi_2Se_3 consist of a single Dirac cone at Γ point on one surface inside the large bulk band gap (~ 0.3 eV) [5,23], which provides an ideal material to study the coupling of spin and orbital textures of surface states. As the starting point, we compare the bulk band structure of Bi_2Se_3 with the previous calculation [5] and find good agreements. The surface states are obtained from the calculation of a freestanding structure with the normal direction [0001], as shown in Fig. 2(a). The blue arrows represent the spin texture, where the spin is mainly lying in the plane near the Dirac point. The spin texture is left handed for the upper Dirac cone and right handed for the lower one, the same as the total angular momentum texture. To understand the underlying physics, we calculate the spin texture for different atomic orbitals. For p_z orbitals, a left-handed helical spin texture is found for the upper Dirac cone and a right-handed texture for the lower Dirac cone, as shown in Figs. 2(b) and 2(c). The schematics of the spin texture are shown in the insets. Here the background color indicates the projection of p_z orbitals, which is isotropic, and the red arrows represent the corresponding in-plane spin texture. The spin texture of p_z orbitals can be reproduced with the expressions $[D^{\pm}_{p_z,\sigma_x}, D^{\pm}_{p_z,\sigma_y}, D^{\pm}_{p_z,\sigma_z}] = \pm\sum_\alpha (u_{0,\alpha} \mp v_{1,\alpha}k)^2[\sin\theta_k, -\cos\theta_k, 0]$ with "$\pm$" for the upper and lower Dirac cone and $\vec{k} = (k, \theta_k)$ in the polar coordinate.

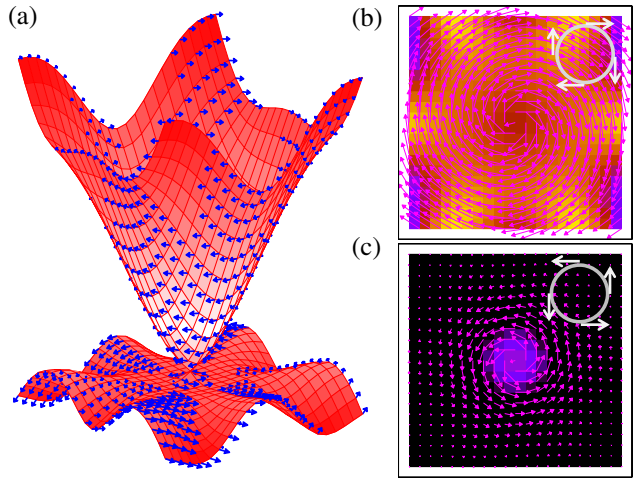

FIG. 2 (color online). (a) The Dirac cone of Bi_2Se_3 on the surface with the normal direction [0001] with the spin texture marked by blue arrows. (b),(c) The projection of the p_z orbital and the related in-plane spin texture for upper (b) and lower (c) Dirac cones. The red color means the projection of p_z orbitals. The red arrows represent the in-plane spin texture related to the p_z orbitals. The insets are the schematics of the spin texture.

The spin textures for in-plane orbitals are shown in Figs. 3(a) and 3(b) for the upper Dirac cone and in Figs. 3(c) and 3(d) for the lower Dirac cone, respectively. We find that the associated spins for p_x and p_y orbitals don't rotate clockwise or anticlockwise around the Dirac point as in the case of p_z orbitals, but instead, they take the form

$$[D^{\pm}_{p_x,x}, D^{\pm}_{p_x,y}, D^{\pm}_{p_x,z}] = \mp\sum_\alpha \frac{v^2_{0,\alpha}}{2}[\sin\theta_k, \cos\theta_k, 0], \quad (7)$$

$$[D^{\pm}_{p_y,x}, D^{\pm}_{p_y,y}, D^{\pm}_{p_y,z}] = \pm\sum_\alpha \frac{v^2_{0,\alpha}}{2}[\sin\theta_k, \cos\theta_k, 0], \quad (8)$$

for small k around the Γ point. The corresponding spin textures are shown schematically in the inset of Figs. 3(a) and 3(c) for p_x orbitals in upper and lower Dirac cones and in the inset of Figs. 3(b) and 3(d) for p_y orbitals. Unlike p_z orbitals, the amplitude of p_x and p_y orbitals for the surface states is not isotropic, but has $2\theta_k$ angular dependence around the Fermi surface, as shown in Fig. 4(c). The red color means the projection of p_x orbital in Fig. 4(a) and p_y orbital Fig. 4(b). Here more red means more p_x character, and more blue means more p_y character. The angular dependence indicates a tangential orbital texture for the upper Dirac cone and a radial orbital texture for the lower Dirac cone, as schematically shown by the inset of Figs. 4(a) and 4(b), respectively. This orbital texture was experimentally observed recently [14]. Furthermore, we

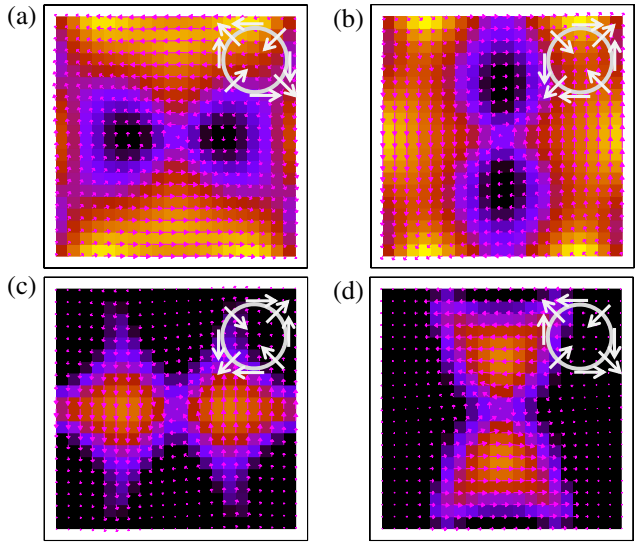

FIG. 3 (color online). (a),(b),(c),(d) The p_x projection on the states of upper (a) and lower (c) Dirac cones, and the p_y projection of upper (b) and lower (d) Dirac cones. The red color means the projection of p_x orbitals in (a) and (c), and the red color means the projection of p_y orbitals in (b) and (d). The red arrows indicate the in-plane spin texture related to the orbitals. The insets are the schematics of the spin texture.

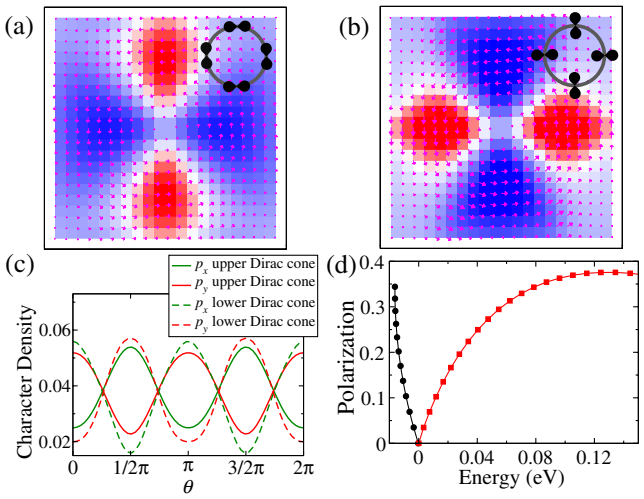

FIG. 4 (color online). (a),(b) The tangential orbital texture with the related in-plane spin texture for the upper Dirac cone (a) and the radial orbital texture for the lower (b) from *ab initio* calculations. The red (blue) color means the projection of p_x (p_y) orbitals. The red arrows represent the total in-plane spin texture related to p_x and p_y orbitals. (c) The p_x and p_y projections onto upper and lower Dirac cones. The solid curves are the p_x and p_y projections for the upper Dirac cone at energy level 0.10 eV, and the dashed curves for the lower Dirac cone at the energy -0.07 eV. The basic feature is the π period which exactly agrees with the prediction by the effective model. (d) Orbital polarization P_{p_x}. The energy of the Dirac point is shifted to be zero. The positive value of the orbital polarization represents the radial orbital texture, and the negative value represents the tangential orbital texture. For clarity, the P_{p_x} for the upper Dirac cone is inversed, marked by the red color. P_{p_x} is exact zero at Dirac point, which indicates the transition point between the tangential and radial orbital textures.

also plot the total spin textures for in-plane orbitals in the same figure, which show a right-handed texture for both upper and lower Dirac cones. All these salient features can be understood by the wave functions (4) and (5). For the upper Dirac cone, although both $|\uparrow_\theta\rangle|p_r\rangle$ and $|\downarrow_\theta\rangle|p_t\rangle$ terms exist in the wave function (4), their associated coefficients are unequal. When $\sum_\alpha(v_{0,\alpha}-u_{1,\alpha}k+w_{1,\alpha}k)^2 > \sum_\alpha(v_{0,\alpha}-u_{1,\alpha}k-w_{1,\alpha}k)^2$, the $|\downarrow_\theta\rangle|p_t\rangle$ term dominates over the $|\uparrow_\theta\rangle|p_r\rangle$ term, dominantly giving a tangential orbital texture coupled to a right-handed spin texture. Similarly, for the lower Dirac cone, when $\sum_\alpha(v_{0,\alpha}+u_{1,\alpha}k+w_{1,\alpha}k)^2 > \sum_\alpha(v_{0,\alpha}+u_{1,\alpha}k-w_{1,\alpha}k)^2$, the $|\downarrow_\theta\rangle|p_r\rangle$ term in the wave function (5) is dominant, yielding a radial orbital texture coupled to a right-handed spin texture. The difference between p_x and p_y orbitals can be calculated directly as $D^{\pm}_{p_x,0}-D^{\pm}_{p_y,0} = \mp 2\cos 2\theta_k \sum_\alpha[(v_{0,\alpha}\mp ku_{1,\alpha})kw_{1,\alpha}]$, which indeed shows a $2\theta_k$ angular dependence, and the total spin textures for in-plane orbitals can be obtained as $[D^{\pm}_x, D^{\pm}_y] = [D^{\pm}_{p_x,x}+D^{\pm}_{p_y,x}, D^{\pm}_{p_x,y}+D^{\pm}_{p_y,y}] = 4[-\sin\theta_k, \cos\theta_k]\sum_\alpha(v_{0,\alpha}\mp ku_{1,\alpha})kw_{1,\alpha}$, which shows a right-handed spin texture when $\sum_\alpha(v_{0,\alpha}\mp ku_{1,\alpha})kw_{1,\alpha} > 0$. Especially, if k gets close to zero, both the total spin texture $[D^{\pm}_x, D^{\pm}_y]$ of the in-plane orbitals and the difference between p_x and p_y orbitals $D^{\pm}_{p_x,0}-D^{\pm}_{p_y,0}$ approach zero, also as shown in Figs. 4(a) and 4(b).

Therefore, there is a transition from a tangential orbital texture in the upper Dirac cone to a radial orbital texture in the lower Dirac cone, switching exactly at the Dirac point. To quantitatively describe this transition, we introduce a polarization quantity

$$P_{p_x}(\pm) = \frac{D_{p_x,0}(\pm,\theta=0)-D_{p_x,0}(\pm,\theta=90)}{D_{p_x,0}(\pm,\theta=0)+D_{p_x,0}(\pm,\theta=90)} \quad (9)$$

with "$\pm$" for upper and lower Dirac cones. The plot of $P_{p_x}(\pm)$ is shown in Fig. 4(d) where the energy level of the Dirac point is shifted to zero. For clarity, we reverse the value of the $P_{p_x}(+)$ for the upper Dirac cone plotted with the red squares. The feature of $P_{p_x}(\pm)$ undoubtedly indicates that the state of the lower Dirac cone forms a radial orbital texture, and the state of the upper Dirac cone forms a tangential orbital texture. The Dirac point is shown to be the exact transition point from the tangential to radial orbital texture. This is exactly the behavior observed in a recent experiment and explained within the first principle calculations [14]. The numerical results fit well to the analytical calculation, with the expression

$$P_{p_x}(\pm) = \mp\frac{2\sum_\alpha(v_{0,\alpha}\mp Eu_{1,\alpha}/\hbar v_f)Ew_{1,\alpha}/\hbar v_f}{\sum_\alpha[(v_{0,\alpha}\mp Eu_{1,\alpha}/\hbar v_f)^2+E^2w^2_{1,\alpha}/\hbar^2v^2_f]}, \quad (10)$$

with the energy E. For small E around Dirac point, $P_{p_x}(\pm) \propto \mp[\sum_\alpha v_{0,\alpha}w_{1,\alpha}/\sum_\alpha(v_{0,\alpha})^2](2E/\hbar v_f)$ shows the linear dependence on energy, as found in Fig. 4(d).

Although in-plane orbitals show different spin textures compared to p_z orbitals, the p_z orbitals (50%) have a larger magnitude for the states near the Dirac point than the p_x and p_y orbitals (together around 30%). Therefore, the spin texture for the whole states show as left handed for the upper Dirac cone and right handed for the lower Dirac cone, the same as that of p_z orbitals, as well as the total angular momentum texture.

In order to detect the spin texture of electrons, the spin-resolved ARPES technology has been developed by taking advantage of spin-dependent scattering processes and precisely measuring the magnitude of the asymmetry in the spin-dependent intensity with perfect spin polarimeters [12]. The nontrivial spin texture of surface states of TIs has been clearly observed by experiments [8–12]. In addition, the orbital character can be detected through the photon polarization selection rules [24] based on the symmetry analysis. With this technology, the orbital texture of surface states of Bi_2Se_3 was reported recently by a polarized ARPES experiment [14]. Therefore, it is possible to combine these two technologies together in an electron

spin-resolved and photon polarized ARPES experiment, with both the spin and orbital textures extracted in the same measurement. The predicted spin-orbital texture can be directly confirmed in this type of experiment, which can explicitly reveal how SOC plays a role in the real material at the atomic level.

We would like to thank Dr. Dan Dessau for sharing his experimental data and for useful discussions, which partially motivated this work. This work is supported by the US Department of Energy, Office of Basic Energy Sciences under Contract No. DE-AC02-76SF00515, the Defense Advanced Research Projects Agency Microsystems Technology Office, MesoDynamic Architecture Program (MESO) through the Contract No. N66001-11-1-4105 and by the DARPA Program on "Topological Insulators–Solid State Chemistry, New Materials and Properties," under the Award No. N66001-12-1-4034.

[1] X.-L. Qi and S.-C. Zhang, Phys. Today **63**, 33 (2010).
[2] J. E. Moore, Nature (London) **464**, 194 (2010).
[3] M. Z. Hasan and C. L. Kane, Rev. Mod. Phys. **82**, 3045 (2010).
[4] X.-L. Qi and S.-C. Zhang, Rev. Mod. Phys. **83**, 1057 (2011).
[5] H. Zhang, C.-X. Liu, X.-L. Qi, X. Dai, Z. Fang, and S.-C. Zhang, Nat. Phys. **5**, 438 (2009).
[6] W. Zhang, R. Yu, H.-J. Zhang, X. Dai, and Z. Fang, New J. Phys. **12**, 065013 (2010).
[7] O. V. Yazyev, J. E. Moore, and S. G. Louie, Phys. Rev. Lett. **105**, 266806 (2010).
[8] D. Hsieh, Y. Xia, L. Wray, D. Qian, A. Pal, J. H. Dil, J. Osterwalder, F. Meier, G. Bihlmayer, C. L. Kane, Y. S. Hor, R. J. Cava, and M. Z. Hasan, Science **323**, 919 (2009).
[9] S. Souma, K. Kosaka, T. Sato, M. Komatsu, A. Takayama, T. Takahashi, M. Kriener, K. Segawa, and Y. Ando, Phys. Rev. Lett. **106**, 216803 (2011).
[10] S.-Y. Xu, L. A. Wray, Y. Xia, F. v. Rohr, Y. S. Hor, J. H. Dil, F. Meier, B. Slomski, J. Osterwalder, M. Neupane, H. Lin, A. Bansil, A. Fedorov, R. J. Cava, and M. Z. Hasan, arXiv:1101.3985.
[11] Z.-H. Pan, E. Vescovo, A. V. Fedorov, D. Gardner, Y. S. Lee, S. Chu, G. D. Gu, and T. Valla, Phys. Rev. Lett. **106**, 257004 (2011).
[12] C. Jozwiak, Y. L. Chen, A. V. Fedorov, J. G. Analytis, C. R. Rotundu, A. K. Schmid, J. D. Denlinger, Y.-D. Chuang, D.-H. Lee, I. R. Fisher, R. J. Birgeneau, Z.-X. Shen, Z. Hussain, and A. Lanzara, Phys. Rev. B **84**, 165113 (2011).
[13] S. R. Park, J. Han, C. Kim, Y. Y. Koh, C. Kim, H. Lee, H. J. Choi, J. H. Han, K. D. Lee, N. J. Hur, M. Arita, K. Shimada, H. Namatame, and M. Taniguchi, Phys. Rev. Lett. **108**, 046805 (2012).
[14] Y. Cao, J. A. Waugh, X.-W. Zhang, J.-W. Luo, Q. Wang, T. J. Reber, S. K. Mo, Z. Xu, A. Yang, J. Schneeloch, G. Gu, M. Brahlek, N. Bansal, S. Oh, A. Zunger, and D. S. Dessau, arXiv:1209.1016.
[15] C.-X. Liu, X.-L. Qi, H. J. Zhang, X. Dai, Z. Fang, and S.-C. Zhang, Phys. Rev. B **82**, 045122 (2010).
[16] L. Fu, Phys. Rev. Lett. **103**, 266801 (2009).
[17] See Supplemental Material at http://link.aps.org/supplemental/10.1103/PhysRevLett.111.066801 for more details of wave functions in the main text.
[18] G. Kresse and J. Hafner, Phys. Rev. B **47**, 558 (1993).
[19] G. Kresse and D. Joubert, Phys. Rev. B **59**, 1758 (1999).
[20] J. P. Perdew, K. Burke, and M. Ernzerhof, Phys. Rev. Lett. **77**, 3865 (1996).
[21] P. Hohenberg and W. Kohn, Phys. Rev. **136**, B864 (1964).
[22] P. E. Blöchl, Phys. Rev. B **50**, 17 953 (1994).
[23] Y. Xia, D. Qian, D. Hsieh, L. Wray, A. Pal, H. Lin, A. Bansil, D. Grauer, Y. S. Hor, R. J. Cava, and M. Z. Hasan, Nat. Phys. **5**, 398 (2009).
[24] A. Damascelli, Z. Hussain, and Z.-X. Shen, Rev. Mod. Phys. **75**, 473 (2003).